



# 1 Improving Statistical Projections of Ocean Dynamic Sea-level Change 2 Using Pattern Recognition Techniques.

3 Víctor Malagón-Santos<sup>1</sup>, Aimée B.A. Slangen<sup>1</sup>, Tim H.J. Hermans<sup>1,2</sup>, Sönke Dangendorf<sup>3</sup>, Marta  
4 Marcos<sup>4</sup>, Nicola Maher<sup>5,6,7</sup>.

5 <sup>1</sup>NIOZ Royal Netherlands Institute for Sea Research, Department of Estuarine & Delta Systems, P.O. Box 140, 4400 AC  
6 Yerseke, the Netherlands.

7 <sup>2</sup>University of Utrecht, Institute for Marine and Atmospheric research Utrecht (IMAU), Utrecht, The Netherlands

8 <sup>3</sup>Department of River-Coastal Science and Engineering, Tulane University, New Orleans, USA.

9 <sup>4</sup>Mediterranean Institute for Advanced Studies (IMEDEA), Spanish National Research Council-University of Balearic Islands  
10 (CSIC-UIB), Esporles, Spain.

11 <sup>5</sup>Cooperative Institute for Research in Environmental Science, University of Colorado, Boulder, CO, USA.

12 <sup>6</sup>Department of Atmospheric and Oceanic Sciences, University of Colorado, Boulder, CO, USA.

13 <sup>7</sup>Max Planck Institute for Meteorology, Hamburg, Germany.

14  
15

16 *Correspondence to:* Víctor Malagón-Santos (victor.malagon.santos@nioz.nl)

17 **Abstract.** Regional emulation tools based on statistical relationships, such as pattern scaling, provide a computationally  
18 inexpensive way of projecting ocean dynamic sea-level change for a broad range of climate change scenarios. Such approaches  
19 usually require a careful selection of one or more predictor variables of climate change so that the statistical model is properly  
20 optimized. Even when appropriate predictors have been selected, spatiotemporal oscillations driven by internal climate  
21 variability can be a large source of model disagreement. Using pattern recognition techniques that exploit spatial covariance  
22 information can effectively reduce internal variability in simulations of ocean dynamic sea level, significantly reducing random  
23 errors in regional emulation tools. Here, we test two pattern recognition methods based on Empirical Orthogonal Functions  
24 (EOF), namely signal-to-noise maximising EOF pattern filtering and low-frequency component analysis, for their ability to  
25 reduce errors in pattern scaling of ocean dynamic sea-level change. These two methods are applied to the initial-condition  
26 large ensemble MPI-GE, so that internal variability is optimally characterized while avoiding model biases. We show that  
27 pattern filtering provides an efficient way of reducing errors compared to other conventional approaches such as a simple  
28 ensemble average. For instance, filtering only two realizations by characterising their common response to external forcing  
29 reduces the random error by almost 60%, a reduction level that is only achieved by averaging at least 12 realizations. We  
30 further investigate the applicability of both methods to single realization modelling experiments, including four CMIP5  
31 simulations for comparison with previous regional emulation analyses. Pattern scaling leads to a varying degree of error  
32 reduction depending on the model and scenario, ranging from more than 20% to about 70% reduction in global-mean root-



33 mean-squared error compared with unfiltered simulations. Our results highlight the relevance of pattern recognition methods  
34 as a tool to reduce errors in regional emulation tools of ocean dynamic sea-level change, especially when one or a few  
35 realizations are available. Removing internal variability prior to tuning regional emulation tools can optimize the performance  
36 of the statistical model and simplify the choice of suitable predictors.

## 37 **1 Introduction**

38 Sea levels are closely linked to the state of the climate. Understanding how increased radiative forcing in the atmosphere will  
39 affect sea-level rise is of utmost importance given the devastating impacts to coastal systems. Global-mean sea level has been  
40 increasing over the 20<sup>th</sup> century (Fox-Kemper, 2021), and its rate has been accelerating over the past decades both globally  
41 (e.g., Dangendorf et al., 2019; Fox-Kemper, 2021; Frederikse et al., 2020; Nerem et al., 2006) and regionally (e.g., Steffebauer  
42 et al., 2022). This acceleration is expected to continue over the next century for all greenhouse gas (GHG) concentration  
43 scenarios (Fox-Kemper et al., 2021) with the potential to further increase widespread impacts in coastal areas (Cooley et al.,  
44 2022). Increased sea levels will change coastal flood risk through expanding areas under permanent inundation, increasing  
45 frequencies of extreme coastal flooding events (Vitousek et al., 2017; Wahl et al., 2017), and modifying tides (Haigh et al.,  
46 2020) and thus potentially increasing the frequency of tidal-induced flooding (Moftakhari et al., 2015). These processes will  
47 not only impact coastal infrastructure and assets (Hinkel et al., 2014) but also alter coastal ecosystems and the services they  
48 provide, from ecosystem value to natural flood risk protection (Cooley et al., 2022). Understanding how global and regional  
49 sea levels evolve under different scenarios will help to better adapt to changing risks and mitigate their potential impacts in  
50 coastal zones (Haasnoot et al., 2019, 2021).

51 Global-mean sea-level change is driven by a combination of processes. The melting of Greenland's and Antarctica's ice sheets,  
52 glaciers and ice caps, changes in land-water storage, and thermal expansion of the ocean are the processes driving global mean  
53 sea-level rise (e.g., Gregory et al., 2019; Fox-Kemper, 2021). Analogously to global warming, sea-level rise is a global concern  
54 but it is not spatially uniform (e.g., Slangen et al., 2017). Four main processes exist that determine regional sea-level change.  
55 First, the redistribution of mass on the Earth's surface, as a result of melting land ice and changes in land-water storage, causes  
56 a regionally variable sea-level change due to gravitational, rotational, and deformational effects (Farrell and Clark, 1976;  
57 Mitrovica et al., 2001). Second, vertical land motion also controls unequal changes in relative sea levels. The viscoelastic  
58 relaxation of the Earth induced by deglaciation following the last glacial maximum, defined as glacial isostatic adjustment  
59 (e.g., Peltier, 1999, 2001) and more local processes driving subsidence (e.g., Nicholls et al., 2021), are the main processes  
60 driving changes in land elevation. Third, (partly wind-driven) ocean circulation, and heat and freshwater fluxes over the ocean,  
61 also known as ocean dynamics (Gregory et al., 2019), change local densities and move water mass around the ocean. Fourth,  
62 changes in sea-level pressure over the oceans, also known as inverted barometer (IB) effects, may lead to regionally varying  
63 rates of sea-level change (Stammer and Hüttemann, 2008)

64



65 This study focuses on ocean dynamic sea-level (DSL) change, which is governed by changes in ocean circulation and density.  
66 DSL is strongly influenced by natural variability, and typically contains the largest spatiotemporal variability among all the  
67 regional sea-level change components. These characteristics make it a crucial component to predict regional sea-level changes  
68 accurately, yet also one that provides significant uncertainty (Couldrey et al., 2021). The effect of climate change on DSL is  
69 typically simulated with General Circulation Models (GCMs), which solve a range of geophysical variables controlling the  
70 Earth's climate system. However, GCMs require vast computational resources, and therefore climate modelling experiments  
71 have been designed for a limited range of GHG concentration scenarios (O'Neill et al., 2017; Riahi et al., 2017; van Vuuren  
72 et al., 2011) within the climate model intercomparison (CMIP) framework (Eyring et al., 2016), so that model differences are  
73 somewhat comparable.

74 To reduce the computational demand, several complementary approaches based on statistical modelling have been proposed.  
75 For instance, regional emulation tools provide a computationally inexpensive alternative for projecting a regional variable and  
76 assessing its response to different forcings. One of the most commonly used emulation approaches for projecting changes in a  
77 regional variable is pattern scaling (Mitchell, 2003; Perrette et al., 2013; Santer et al., 1990), which consists of relating a local,  
78 grid-point variable (predictand) to one or a few global-mean change variables (predictors) via regression. Based on that  
79 statistical relationship, a change in a regional variable can be emulated by projecting the global-mean variables via simpler  
80 climate models (Goodwin et al., 2018; Meinshausen et al., 2011; Millar et al., 2017; Smith et al., 2018)

81 Here, we build on the approach proposed by Bilbao et al. (2015), who applied a linear pattern scaling approach to assess the  
82 ensemble mean DSL computed from five CMIP5 models and their simulations of several variables describing global changes,  
83 including Global Surface Air Temperature (GSAT), Global-Mean Thermosteric Sea-Level Rise (GMTSLR), and ocean-  
84 volume mean temperature. While GSAT turned out to be the best predictor of 21<sup>st</sup>-century DSL change in a high emissions  
85 scenario (Representative Concentration Pathway (RCP) 8.5), ocean-volume mean temperature and GMTSLR outperformed  
86 the rest of variables considered in lower emissions scenarios (RCP 2.6 and 4.5). As the surface ocean layer responds quicker  
87 to air temperature changes than the deeper ocean layer, they speculated that surface warming had a more important role relative  
88 to deep warming in a high emissions scenario. Based on Bilbao et al. (2015)'s findings, Yuan and Kopp (2021) used the same  
89 set of CMIP5 models to develop a bivariate pattern scaling approach, accounting for the surface and deep ocean layers  
90 separately. Their goal was to capture the different delayed response of those two layers by using GSAT and global-mean deep  
91 ocean temperature changes as predictors. By employing a bivariate pattern scaling approach, Yuan and Kopp (2021) reported  
92 a reduction of the predicted DSL error for the period 2271-2290 of 36%, 24%, and 34% for RCP 2.6, 4.5, and 8.5, respectively,  
93 compared to a univariate approach based on only GSAT.

94 The aforementioned studies highlight the importance of selecting appropriate predictors to attain an optimized regional  
95 emulator of DSL, and how accounting for different processes driving DSL change (in different layers of the ocean) can help  
96 further improve emulator performance. While designing a regional emulator based on performance metrics may provide  
97 insights into the global processes driving DSL changes, this process can be obscured by other drivers of emulator error. In  
98 particular, random errors contained in the regression forming the pattern scaling approach, are assumed to be mostly caused



99 by internal climate variability (Bilbao et al., 2015) and may be a source of large uncertainty. Thus, if random errors are not  
100 minimized prior to emulator training with GCM simulations, their presence could impair a proper selection of global predictors,  
101 such that it would be uncertain whether an increase in model performance is due to an appropriate selection of predictors or  
102 an artifact of natural variability causing a biased selection. In previous studies, this effect has been minimized by computing  
103 30-year means, assuming this cancels out natural variability. This step, however, entails a substantial loss of data and does not  
104 guarantee natural variability is optimally subtracted, and residual natural variability, for instance caused by long-memory  
105 processes (e.g., Becker et al., 2014; Dangendorf et al., 2014), can remain.

106 We therefore propose to take a different approach to separate internal variability from the response driven by external radiative  
107 forcing in the Earth, by employing state-of-the-art modelling experiments specifically designed to do so. These are known as  
108 Single-Model Initial Condition Large Ensembles (SMILES) and consist of a set of simulations with the same forcing but with  
109 the variability evolving in a different phase (Deser et al., 2020). These realizations can be combined through different methods  
110 (e.g., Frankcombe et al., 2015) so that internal variability cancels out. However, conventional approaches such as computing  
111 the ensemble mean or linear trends are not the most efficient tools to do so and tend to lead to the loss of much of the  
112 information gained from running large ensembles (Wills et al., 2020). Other methods based on pattern recognition via  
113 Empirical Orthogonal Functions (EOFs) exploit spatial covariance information to remove internal variability more efficiently  
114 (Wills et al., 2020) and have demonstrated to provide a superior agreement between observations and simulations than an  
115 ensemble average (Marcos and Amores, 2014). These types of efficient methods for removing internal variability hold potential  
116 to benefit emulation experiments of DSL for which the number of simulations is limited.

117 The aim of this study is to characterise the importance of natural variability as a driver of random errors in statistically based  
118 (pattern-scaled) projections of DSL change. To achieve this aim, we will compare different pattern recognition techniques,  
119 including Signal-to-Noise Maximising (S/N M) EOF pattern filtering (Wills et al., 2020) and Low Frequency Component  
120 Analysis (LFCA, Wills et al., 2018, 2020). We will use these techniques to truncate natural variability in DSL simulations  
121 from the MPI-GE SMILE (Maher et al., 2019), and explore their applicability to single realization modelling experiments,  
122 including a set of CMIP5 simulations used in previous pattern scaling studies. In this paper, we particularly aim to attain the  
123 following objectives:

124

- 125 1) Use a large ensemble (MPI-GE) to determine the forced pattern and examine to which extent pattern recognition  
126 techniques isolate the forced response in DSL change more efficiently than conventional methods (Section 4.1)
- 127 2) Determine the error reduction in pattern scaling of DSL provided by pattern recognition methods relative to more  
128 conventional methods (Section 4.2).
- 129 3) Test whether filtering improves pattern scaling in single-realization modelling experiments of DSL (Section 4.3).



## 130 **2 Climate model data and pre-processing**

131 Separating natural variability from the forced response is key for detection and attribution studies in climate change (Labe and  
132 Barnes, 2021) and to understand its effects on the climate system (Deser et al., 2020; Mankin et al., 2020). However, the  
133 combination of distinct GCMs to analyse internal variability should be performed with caution, as this may conflate internal  
134 variability with model biases (Maher et al., 2021b). In recent literature, this has motivated the development and use of SMILES,  
135 which branch each realization at a different model stage in the pre-industrial control simulation (Danabasoglu et al., 2020;  
136 Deser et al., 2020; Fasullo et al., 2020; Kay et al., 2015; Maher et al., 2019, 2021a; Mankin et al., 2020). This results in  
137 simulations with the same forced response but with variability evolving in a different phase, enabling a separation of the  
138 variability from the forced response.

139 From the available SMILES (Deser et al., 2020; Maher et al., 2021a), we decided to use the Max-Planck Institute Grand  
140 Ensemble (MPI-GE; Maher et al., 2019) because it contains the largest number of ensemble members available (100) in a  
141 SMILE. Moreover, the realizations are available for historical simulations and different RCP scenarios (RCP 2.6, 4.5, and 8.5)  
142 up to 2100 together with an extended pre-industrial control simulation. The MPI-GE ensemble design is based on macro-  
143 initialization, where 100 distinct coupled initial conditions are sampled from well separated starting dates in the pre-industrial  
144 control, such that ensemble members start from different ocean and atmospheric states. This procedure allows assessing  
145 uncertainty due to initial conditions differences in large scale aspects of the climate system as well as uncertainty in future  
146 model climate due to the non-linear nature of the climate system (Hawkins et al., 2016; Stainforth et al., 2007). Macro-  
147 initialized ensembles are therefore better suited than ‘micro’ ensembles, which are the ones where atmospheric initial  
148 conditions are perturbed, to sample uncertainty in an initialized framework, facilitating an assessment of natural variability  
149 within a model.

150 Additionally, we use four CMIP5 models that were used in previous studies of DSL pattern scaling (Bilbao et al., 2015; Yuan  
151 and Kopp, 2021), including GISS-E2-R, HadGEM2-ES, IPSL-CM5A-LR, and MPI-ESM-LR. These four GCMs were selected  
152 in the afore-mentioned studies because they were used to calibrate the parameters of the simple climate model used by Geoffroy  
153 et al. (2013a, b), which facilitated the design of their emulation tool. Also, these models provide multi-century data (up to  
154 2300) in three emissions scenarios, granting an assessment of the suitability of pattern scaling for long-term projections. We  
155 use them here for comparison purposes.

156 The focus of this study is on DSL, which in CMIP models is also known as ‘zos’ (Griffies et al., 2016) and defined at each  
157 location and time as the difference between local sea-surface height relative to the geoid, and its global mean over the ocean  
158 area (GMTSLR, or ‘zostoga’ in CMIP experiments). Hence, by definition, DSL, or zos, varies locally due to ocean circulation  
159 and horizontal gradients, but its global mean is zero at every time step. Both zos and zostoga are often expressed in terms of  
160 changes relative to a control state, expressing them as differences in relation to a baseline period. Moreover, sea level is  
161 influenced by atmospheric pressure anomalies, which is known as the IB effect. DSL simulations from GCMs do not include



162 the effect of sea-level pressure on sea level and such effect is not subject of study in our analysis, hence it is not considered  
163 here.

164 Since we are interested in assessing the forced response in DSL for historical and future GHG emissions we will use zos from  
165 a range of GCMs for historical and future radiative forcing scenarios, including RCP 2.6, 4.5, and 8.5 (Meinshausen et al.,  
166 2011). Once the forced DSL has been characterized, we will proceed to pattern scale each model and scenario using GMTSLR  
167 (zostoga) from their respective GCM simulation. Among other potential global predictors, we chose GMTSLR as it is closely  
168 related to DSL, and it has been successfully used in previous pattern scaling analysis of DSL (e.g., Bilbao et al., 2015; Thomas  
169 and Lin, 2018). We refrain from testing other global variables as predictors to ease comparing models and scenarios, and  
170 determining to which extent pattern filtering reduces statistical error via reducing internal variability.

171 In this study, we are particularly interested in removing interannual variability, thus we compute annual mean zostoga and zos  
172 time series from the raw monthly mean GCM data. In addition, since GCMs are run for a few centuries and the deep ocean  
173 usually takes millennia to reach an equilibrium, both zos and zostoga are subject to model drift (Sen Gupta et al., 2013). Model  
174 drift in the historical and scenario simulations can be corrected for by subtracting the smoothed long-term change of the pre-  
175 industrial control run. To avoid contaminating the drift correction with natural variability, ideally the full length of the control  
176 run is used to determine the drift (Sen Gupta et al., 2013). Therefore, to dedrift the historical and scenario simulations of  
177 zostoga and zos (the latter on a grid cell by grid cell basis) we first fit a quadratic polynomial to the full pre-industrial control  
178 simulations of these variables. Then, we evaluate and subtract the polynomial fit over the time period in which the pre-industrial  
179 control run and historical and scenario runs overlap, as identified by the branch times of the different simulation realizations  
180 and their length, from the historical and scenario runs. Similar to what was found by Hermans et al., (2020) and Hobbs et al.  
181 (2016), fitting a linear or quadratic polynomial to the pre-industrial control simulations yields little difference for the drift-  
182 correction of the zostoga simulations of GISS-E2-R, HadGEM2-ES, IPSL-CM5A-LR, and MPI-ESM-LR. However, in the  
183 pre-industrial simulation of MPI-GE, the increase of zostoga behaves non-linearly and levels off toward the branching time of  
184 ensemble member 40, so we only dedrift ensemble members 1 to 39. For zos, some differences are found between linear and  
185 quadratic drift correction depending on the model, variant, and location. We assume linear dedrift is suitable for our  
186 purpose, since we verified that the dedrift does not substantially affect the pattern scaling performance and it is tedious to  
187 assess the best fit on a grid-point basis. After dedrift, the area-weighted mean of zos is removed at each timestep, and the  
188 resulting fields are bilinearly regridded to a common 1 by 1 degree grid.

## 189 **3 Methods**

### 190 **3.1 Pattern recognition techniques**

191 Both S/N M EOF pattern filtering and LFCA are based on a technique called linear discriminant analysis to identify spatial  
192 features, as defined by linear combinations of EOFs, that maximize a type of variance describing a ‘signal’. This technique  
193 allows to distinguish that signal from noise existing due to internal variability or between realizations. The difference between



194 S/N M EOF and LFCA lies in their definition of what type of variance constitutes the signal and the noise. The following  
195 subsections briefly explain the pattern filtering methods mentioned above. For a more detailed description, the reader is referred  
196 to Wills et al. (2018, 2020).

### 197 **3.1.1 S/N-maximizing pattern filtering**

198 S/N M EOF pattern filtering detects anomaly patterns that maximize a particular type of variance defined as signal (Schneider  
199 and Griffies, 1999; Ting et al., 2009; Venzke et al., 1999). One way of doing so is to assess a simulation of forced climate  
200 change relative to a preindustrial control (DelSole et al., 2011; Marcos and Amores, 2014). This is advantageous in single-  
201 realization GCM experiments, as it only requires one forced realization and one preindustrial control run. However, this could  
202 neglect the forced response when external forcing only affects the phase of a mode of internal variability (Wills et al., 2020).  
203 Another way of applying this method, which would avoid phase neglect issues, is to use various SMILE realizations with  
204 the same forcing to find anomaly patterns where different ensemble members agree on the temporal evolution. These patterns  
205 with high signal-to-noise ratio form the forced response as simulated by the GCM, and the variability not described by those  
206 can be then truncated from the dataset. S/N M EOF pattern filtering finds anomaly patterns associated with time series  $t_k$  that  
207 maximize the ratio of (ensemble mean) signal to total variance:

$$208 \quad 209 \quad S_k = \frac{\langle t_k \rangle^T \langle t_k \rangle}{t_k^T t_k}, \quad (1)$$

210  
211 where angle brackets represent an ensemble average and  $k$  represents a given pattern. These time series (l.h.s. of Fig. 2, for  
212 example) are determined by projecting a fingerprint pattern  $u_k$  obtained from the EOF analysis (see below) (r.h.s. of Fig. 2, for  
213 example) onto the ensemble data matrix  $X$ :

$$214 \quad 215 \quad t_k = Xu_k, \quad (2)$$

216  
217 The ensemble data matrix  $X$  is defined as  $n \cdot n_e \times p$ , where  $n$  is the length of time series,  $n_e$  is the number of ensemble members,  
218 and  $p$  is the spatial dimension (i.e., longitude and latitude), and is created by concatenating the  $n_e \times p$  data matrices  $X_i$  from  
219 each ensemble member ( $i$ ) in the time dimension. All data matrices  $X_i$  from each ensemble member are weighted by the square  
220 root of grid cell area, so that the covariance matrix is also area weighted.

221 The identified patterns should correspond to variability that occurs within the ensemble. To abide by this requirement, the  
222 fingerprint patterns  $u_k$  are defined as linear combinations of the  $N$  leading ensemble EOFs  $a_k$ , with normalized weight vectors  
223  $e_k$ , being  $\sigma$  the standard deviation (SD):

224



225 
$$u_k = \begin{bmatrix} a_1 & a_2 & \dots & a_N \\ \sigma_1 & \sigma_2 & \dots & \sigma_N \end{bmatrix} e_k, \quad (3)$$

226

227 Linear-combination coefficients  $e_k$  that give  $u_k$  and  $t_k$  that maximize  $s_k$  can be obtained by combining (2) and (3) into (1) (see  
228 Wills et al. (2020) for more details on solving the ensemble EOFs  $a_1$  eigenvectors of ensemble mean covariance). The S/N  
229 maximizing patterns  $v_k$  are estimated by regressing the ensemble data matrix  $X$  onto each  $t_k$ .

230

231 
$$v_k = X^T t_k = X^T X u_k = [\sigma_1 a_1 \quad \sigma_2 a_2 \quad \dots \quad \sigma_N a_N] e_k, \quad (4)$$

232

233 The S/N patterns (S/N Ps) are sorted by the ratio  $s_k$ , obtaining the leading S/NPs patterns of forced response within the  
234 ensemble. Once the leading S/NPs have been determined, a dataset that excludes internal variability and contains the forced  
235 response ( $X_{S/NP}$ ) can be constructed by truncating the patterns and associated temporal response from the M leading S/NPs:

236

237 
$$X_{S/NP} = \sum_{k=1}^M t_k v_k^T, \quad (5)$$

238

239 To apply S/N M EOF pattern filtering, we must choose two parameters: 1) the number of EOFs retained (N), and 2) the number  
240 of S/N Ps used to compose the forced response (M). Following the approach by Wills et al. (2020), we choose N to retain  
241 between 75% and 95% of the total variance. We use a block bootstrapping approach to determine M, which consists of taking  
242 block (for example, decadal) samples with replacement from the ensemble members to construct dimensionally equivalent  
243 randomized ensembles where the forced response timing of their realizations should not agree with one another. Here, we  
244 choose 30-yr blocks to distinguish forced patterns from internal variability, so that most of internal variability in DSL is  
245 excluded. S/N EOF pattern filtering is then applied to randomized ensembles and the  $s_k$  value of the pattern with the highest  
246 S/N ratio is taken as a threshold. This allows us to obtain a distribution of  $s_k$  values (one for each randomized ensemble  
247 produced) from which a desired confidence level can be estimated. S/N M EOF patterns with a higher  $s_k$  value than the  
248 threshold can be considered as part of the forced response with the chosen confidence level. In contrast, there is no sufficient  
249 statistical evidence to include patterns with a lower  $s_k$  value in the forced response, and those are considered noise (internal  
250 variability).

### 251 3.1.2 Low Frequency Component Analysis

252 While S/N M EOF has demonstrated to be particularly useful to isolating the forced response when various ensemble members  
253 are available, the advantage of LFCA is that it can analyse the forced response in a single ensemble member (Schneider and  
254 Held, 2001; Wills et al., 2018). The failure to detect some signals in surface air temperature (Wills et al., 2020), such as those  
255 driven by volcanic activity and in some changes in the seasonal cycle is the main disadvantage of this method being document  
256 in literature.





257 LFCA uses a similar methodology as S/NP M EOF pattern filtering, but detects anomaly patterns associated with time series  
258  $t_k$  that maximize the ratio of low-frequency signal to total variance:

259

$$260 \quad r_k = \frac{\widetilde{t}_k^T \widetilde{t}_k}{t_k^T t_k}, \quad (6)$$

261

262 Variations that make it through a low-pass filter (denoted by a tilde), constitute the low-frequency signal (forced response).  
263 Here, we apply a linear Lanczos filter (Duchon, 1979) with a 30-yr lowpass filter, so only longer-scale variability is included.  
264 Similar to S/NP M EOF, patterns  $v_k$  and their time series  $t_k$  are determined by Eqs. (4) and (2), respectively. Low frequency  
265 patterns are then sorted by the ratio  $r_k$ , so that the leading patterns are those that maximize the ratio of low-frequency to total  
266 variance. The leading anomaly patterns are used to construct a dataset  $X_{LFP}$  containing only the variability captured by the  
267 leading M low frequency patterns:

268

$$269 \quad X_{LFP} = \sum_{k=1}^M t_k v_k^T, \quad (7)$$

270

### 271 3.2 Pattern scaling

272 Pattern scaling is usually based on grid-point regression against a global variable, and it assumes that a regional change in DSL  
273 can be explained by global changes of the predictor(s) of choice. Previous studies have shown such relationships can be a  
274 reasonable approximation for different variables of the climate system. For instance, local surface air temperature change  
275 (Collins et al., 2013; Hawkins and Sutton, 2012) and local precipitation (Osborn et al., 2016) have successfully been linked to  
276 GSAT change. Regional emulation based on pattern scaling assumes that patterns of local response to external forcing remains  
277 constant (Tebaldi and Arblaster, 2014), an assumption that can lead to errors (Wells et al., 2022). However, its simplicity and  
278 transferability to many regional variables have made it a popular approach for exploring regional changes in climate change  
279 studies (Bilbao et al., 2015; Fox-Kemper, 2021; Herger et al., 2015; Mitchell, 2003; Osborn et al., 2016; Perrette et al., 2013;  
280 Tebaldi and Arblaster, 2014; Thomas and Lin, 2018; Wells et al., 2022; Wu et al., 2021; Yuan and Kopp, 2021).

281 Once we have identified the forced DSL within an ensemble of realizations or a single simulation (as outlined in Section 3.1),  
282 we will use this forced response as a predictand in our statistical model for projecting regional DSL. There are different forms  
283 of pattern scaling, mostly differing in the number of predictors included in the analysis (e.g., univariate, Bilbao et al., 2015;  
284 bivariate, Yuan & Kopp, 2021). Here, for simplicity and to ease comparison between raw (de-drifted) DSL and its pattern-  
285 filtered equivalent, we only test pattern scaling based on GMTSLR (or zostoga) as a predictor. The univariate case of pattern  
286 scaling for relating DSL with GMTSLR can be described by the following linear regression relationship:

287



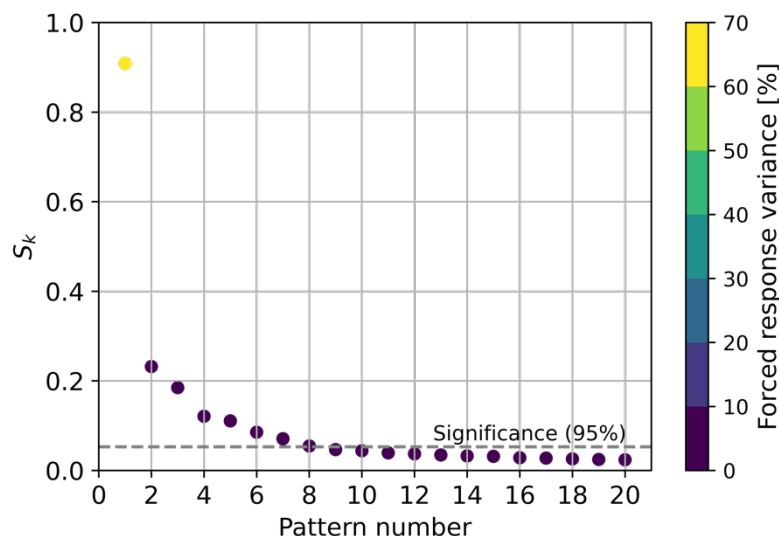
288 
$$\zeta(t, x, y) = \alpha(x, y) \bar{\eta}(t) + b(x, y) + \varepsilon(t, x, y) \quad (10)$$

289  
290 Where  $\zeta$  and  $\bar{\eta}$  denote DSL and GMTSLR, respectively. Longitude and latitude are represented by  $x$  and  $y$ , whereas  $t$  denotes  
291 time.  $\alpha$  is a spatial pattern that captures the scaling relationship between DSL and GMTSLR, and  $b$  is an intercept term, both  
292 being only a function of location.  $\varepsilon$  is a residual term regarded as random noise and often assumed to be driven by internally  
293 generated variability (Bilbao et al, 2015).

## 294 4 Results & Discussion

### 295 4.1 Forced response in MPI-GE and efficiency of pattern filtering.

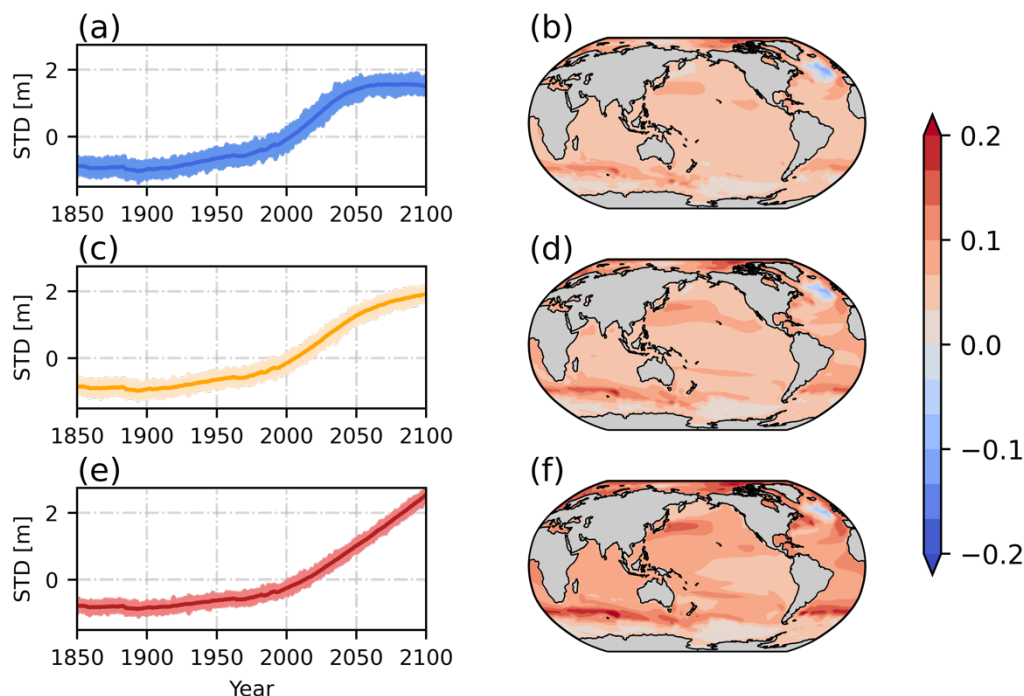
296 In this section, we focus on determining the forced response in DSL within a SMILE (MPI-GE) using S/N M EOF pattern  
297 filtering and show the efficiency of the latter to remove internal variability compared to conventional approaches. To construct  
298 the forced response based on S/N P, we follow the block-bootstrapping approach described in Section 3.1.1. we define blocks  
299 in terms of thirty years, so most natural variability in DSL is excluded. 30-yr block samples are taken from the 100 historical  
300 realizations of the MPI-GE to construct 20 randomized ensembles. A value of 20 is chosen because increasing it further do not  
301 lead to substantial changes in the estimation of the 95<sup>th</sup> percentile of  $S_k$ . The estimated ratio  $S_k$  (Eq. 1) for a 95 % confidence  
302 level is 0.08, leading to a total of eight patterns that can be considered as part of the forced response at such a confidence level  
303 (Figure 1).



304  
305



306 **Figure 1:** Signal fraction of the leading S/N M EOF patterns along with their respective explained forced response variance.  
307 The significance level (95%) computed using 30-year block-bootstrapping is represented as a dashed line.  
308 Even though patterns constructed based on EOFs are created from mathematical constraints, known physical processes can be  
309 identified in some patterns. For instance, the S/N M EOF pattern with the highest  $S_k$  value pattern 1, Fig. 2) explains 62% of  
310 the forced response variance (Fig. 1) and is similar to the main forced pattern of DSL change field driven by increased radiative  
311 forcing due to increased GHG emissions. There is a zonal dipole in the Southern Ocean, with decreased and increased sea level  
312 relative to the mean below and above  $50^\circ\text{S}$ , respectively (e.g., Frankcombe et al., 2013). Another dipole structure is found in  
313 the North Atlantic with a decreased DSL in the north compared to an increased DSL in the southern section, a feature which  
314 appears to disagree with some models (e.g., Bouttes et al., 2014). Nonetheless, the North Atlantic Ocean is an area of large  
315 model spread in both CMIP5 and CMIP6 models (Lyu et al., 2020), which suggests the representation of such zonal dipole  
316 may be model dependent. Other relevant features include a large DSL rise in the Beaufort Sea and an increased DSL in the  
317 North-West Pacific Ocean. Most of these features agree with those documented among CMIP6 and earlier models (Church et  
318 al., 2013; Ferrero et al., 2021; Landerer et al., 2007; Lowe and Gregory, 2006; Lyu et al., 2020; Slangen et al., 2014). Patterns  
319 are similar between RCP scenarios, mainly differing on their intensity.  
320 The three following resulting patterns (patterns 2, 3 and 4, Fig. S1, S2 and S3) represent between 4-1% (Fig. 1) of the forced  
321 response variance and, although with a much lower importance than pattern 1, when combined together represent non-linear  
322 processes that start to have an effect in DSL after 2050. Patterns 5, 6, 7 and 8 (Fig. S4, S5, S6, and S7) explain between 1-  
323 0.7% of the forced response variance (Fig. 1) and show small perturbations and regional responses that appear to be linked to  
324 volcanic eruptions. The patterns number 9 and beyond explain a variance of less than 0,6% and, since their  $S_k$  value is not  
325 statistically significant at the 95% level, they could be caused by random chance.  
326



327

328

329

330

331

332

333

334

335

336

337

338

339

340

341

342

343

344

345

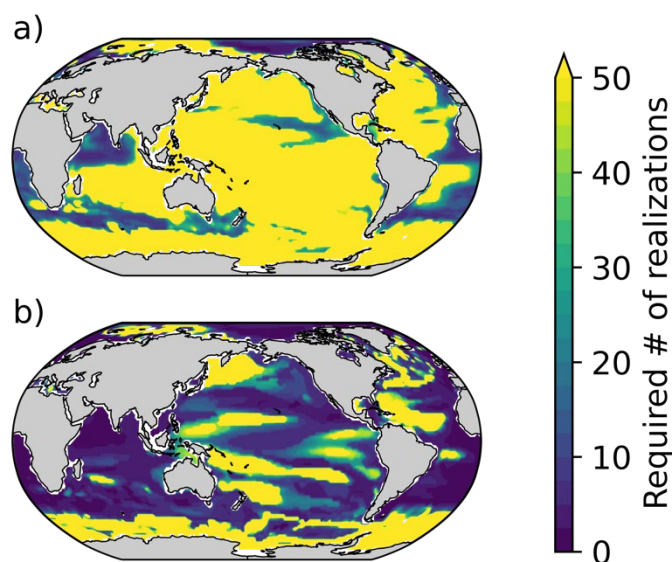
**Figure 2:** Time evolution in terms of SD (a, c, and e, respectively) and associated S/N M EOF pattern number 1 for RCP 2.6, 4.5, and 8.5 (b, d, and f respectively). Light coloured lines in a, c, and d represent SD anomalies from ensemble members, whereas dark coloured lines depict ensemble mean evolution of the pattern. In the historical + RCP scenarios DSL is calculated relative to the mean of 1993–2012

We first compare pattern filtering techniques to conventional methods, in particular an ensemble mean, to isolate the forced response in DSL. For the comparison, we follow the approach used by Wills et al. (2020), where the ensemble is divided into two sub-ensembles: one is used for testing (estimate ensemble) and the other is left for reference (reference ensemble). This leaves us with two 50-member sub-ensembles, where all 50 members in the reference sub-ensemble are used to estimate the forced response by either using ensemble averaging or S/N M EOF pattern filtering and is considered ground truth. The other (estimate) 50-member ensemble is also used to estimate the forced response, but this is performed 49 times by increasing the number of members included in the analysis from 2 to 50. This procedure enables an evaluation of the number of ensemble members needed in the estimate sub-ensemble to characterize the forced response based on explained variance (i.e.,  $r^2$ ) in the reference sub-ensemble. To consider sampling uncertainty, this process is repeated ten times for random choices of realizations, taking the median value of all iterations.

When simple averaging is used, we find that 50 members are not sufficient to constrain at least 80% of the forced response variance of the reference ensemble over most of the ocean surface (Fig. 3a). In contrast, S/N M EOF pattern filtering characterises the forced response more efficiently than simply averaging, as it requires a much smaller number of realizations



346 to remove natural variability (Fig. 3b). While the grid-point median value of the number of ensemble members required is 50  
347 or more when using simple averaging, the median estimate for the filtering method is reduced to eight. Large areas of the  
348 ocean benefit from filtering and there are significant reductions, especially the Indian Ocean, South and Northwest Atlantic  
349 Ocean, as well as large areas in the Pacific Ocean (Fig. 3b). Other areas, however, remain over the 50-member threshold to  
350 explain forced response variance after filtering. Those areas are mostly found where strong western boundary currents exist  
351 (Imawaki et al., 2013), as well as in areas influenced by the Antarctic Circumpolar Current (Rintoul et al., 2001). In those  
352 locations, variability is higher, and a larger number of realizations is needed to characterize it. Yet, there clearly is an advantage  
353 in using S/N M EOF over simple averaging methods, as less realizations are required to explain a significant part of the forced  
354 response in DSL, which means that the forced response can also be determined in models with smaller ensembles.



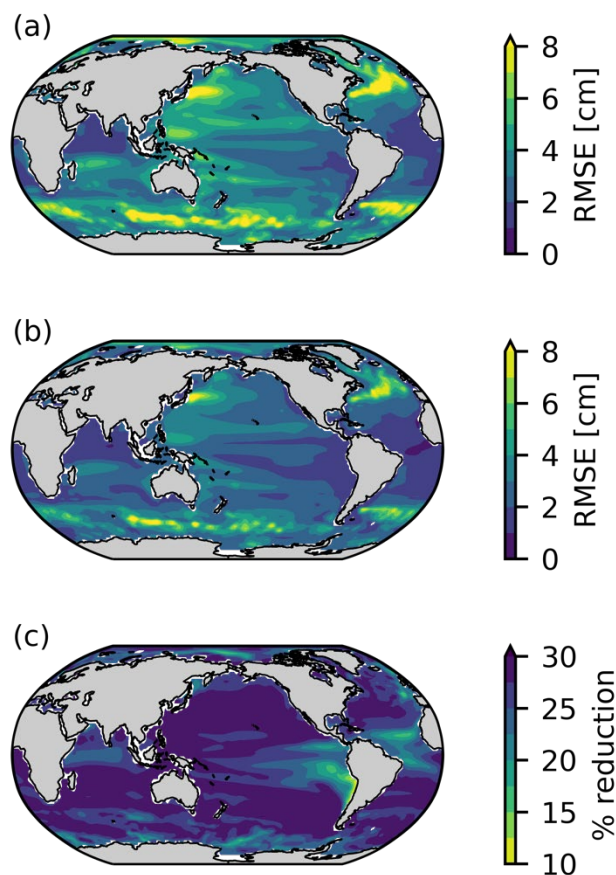
355  
356  
357 **Figure 3.** The number of ensemble members (realizations) needed to explain at least 80% of the forced response variance  
358 using an ensemble average (a) and using S/N M EOF pattern filtering (b) for RCP 2.6. The reference dataset is an average (a)  
359 or S/M EOF-filtered sub-ensemble (b) of 50 members which does not share realizations with the sub-ensemble used for  
360 estimation. Values represent the median of ten random choices of realizations sampling for both estimate and reference sub-  
361 ensembles. Note that bright yellow indicates more than 50 ensemble members required.

#### 362 4.2 Improved Pattern Scaling Using SMILES

363 In this section, we demonstrate how S/N M EOF pattern filtering can increase the capabilities of statistical approaches for  
364 explaining DSL based in GMTSLR by reducing internal variability within SMILES. For comparison, we first show pattern  
365 scaling performance when using single realizations and how conventional methods (ensemble mean) reduces RMSE when



366 using a couple of realizations instead. Second, we examine S/N M EOF as a method for reducing RMSE more efficiently. We  
367 compare regional RSME from both ensemble mean and pattern filtering on only two realizations to allow an assessment of the  
368 areas that benefit the most from filtering when a few simulations are available. Lastly, we contrast how both ensemble mean  
369 and S/N M EOF pattern filtering reduce global mean RMSE as the number of realizations included in the analysis is increased.  
370 As pattern scaling is performed on a grid-point basis, regression performances can be location dependent (Fig. 4a). Despite  
371 such regional variations, we found not substantial differences between GHG scenarios for both the regional and global mean  
372 RMSE estimates when pattern scaling DSL simulations extending up to 2100. Thus, results shown and discussed here are  
373 pertinent to the historical+RCP2.6 scenario for illustrative purposes, unless otherwise stated. When applying pattern scaling  
374 on a single realization of DSL from MPI-GE, the area-weighted, ensemble average RMSE is 3.78 cm, a value which is similar  
375 to previous estimates from studies performed on some of the CMIP5 models (Bilbao et al., 2015; Yuan and Kopp, 2021).  
376 However, pattern scaling performance shows a large spatial variability, ranging from 1.13 to 14.95 cm regionally (Fig. 4a).  
377 High RMSE values (i.e., lower regression performance) can be found in places subject to non-linear mesoscale processes  
378 driven by strong currents, coinciding with the places where the S/N M EOF technique requires many realizations to explain at  
379 least 80% of the forced response variance (Fig. 3b). These are the Antarctic Circumpolar Current (Southern Ocean) or western  
380 boundary currents, including the Gulf Stream (West North Atlantic), and Agulhas Current (South Africa), the Kuroshio Current  
381 (West North Pacific), and at the Brazil-Malvinas Confluence (West South Atlantic). Low RMSE values are found in the more  
382 stable eastern boundary currents, such as the Humboldt (Peru) Current, and in equatorial locations where DSL is relatively less  
383 influenced by large modes of climate variability (e.g., Equatorial Atlantic and Indian Ocean).  
384 Despite its inefficiency, using an ensemble average cancels out some of the natural variability that varies in a different phase  
385 between realizations. When using a 2-member ensemble mean, RMSE reduction is observed both globally and regionally: The  
386 area-weighted average RMSE estimate is reduced from 3.78 to 2.77 cm (27% reduction) when two ensembles are used, with  
387 regional values ranging from 0.87 to 11.00 cm (Fig. 4b). This translates to increased statistical model capabilities within the  
388 entire model domain. While grid-point RMSE reduction ranges from 10 to 30%, the majority of the ocean benefits from a  
389 decrease of more than 25% due to the removal of some of the internal variability (Fig. 4c). Locations experiencing a lower  
390 improvement in regression performance include those that already performed relatively well prior averaging and those with a  
391 high internal variability.



392  
393 **Figure 4.** Regional pattern scaling performance based on regression RMSE when one realization (a) and a two-member  
394 ensemble average (b) are used in the univariate regression. Sampling uncertainty is accounted for in (a) by averaging RMSE  
395 from pattern scaling performed individually to the 100 realizations, whereas in (b) random pairs (without replacement) are  
396 taken to for the two-member ensemble average. The difference in regression performance between (a) and (b) is shown in (c)  
397 in terms of percentage. Results are shown for RCP 2.6 as an example.

398  
399 To compare how S/N M EOF pattern filtering improves pattern scaling as opposed to averaging, we take two ensemble  
400 members from the MPI-GE historical+RCP2.6 experiment and proceed to remove their natural variability by pattern  
401 filtering. The 2-member pattern-filtered DSL (Fig. 5a) shows an improved RMSE with similar regional structures compared  
402 to its averaged counterpart (Fig. 4b), featuring higher values in western boundary currents and Southern Ocean. Nonetheless,  
403 the overall improvement is apparent in all areas: the global estimated RMSE from the regression decreases almost 60% from  
404 an average value of 2.77 to 1.12 cm (Fig. 5 c and d). Regionally, RMSE ranges from 0.39 to 6.05 cm when filtering is  
405 applied on two ensemble members (Fig. 5a and c). The differences between averaged and filtered approaches are substantial

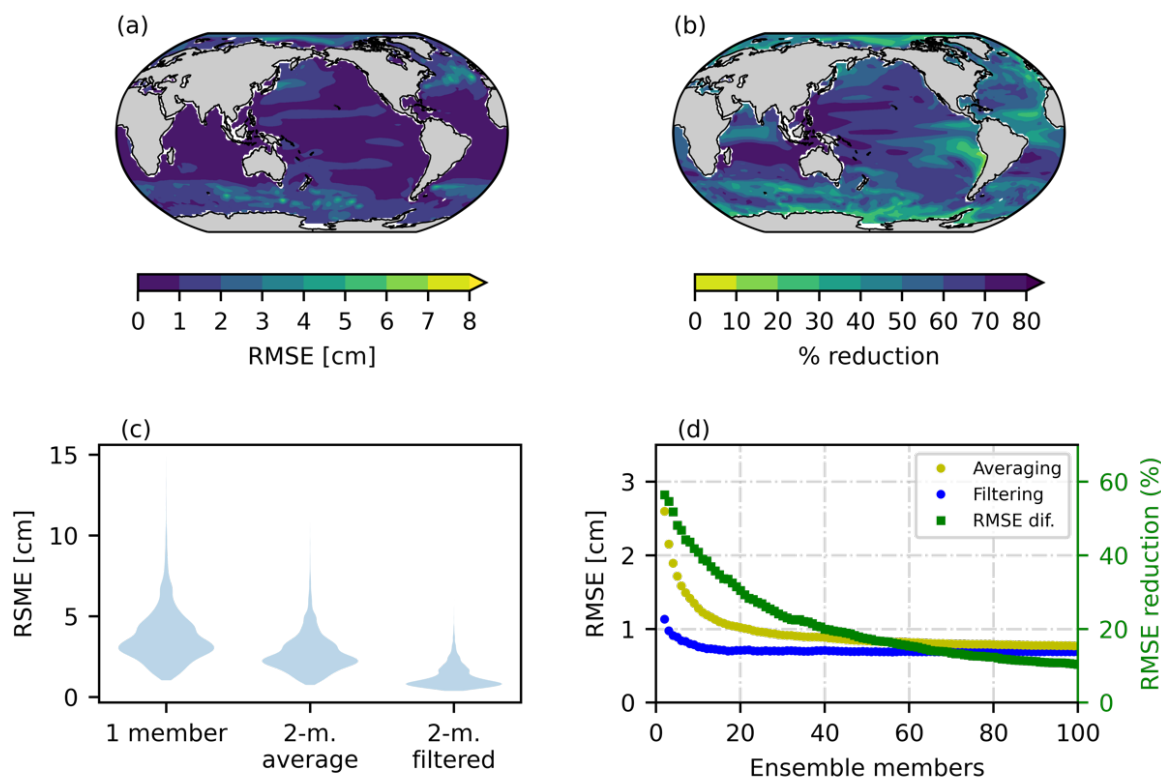


406 and location dependent, with filtering yielding a decrease in RMSE ranging from 12% to about 80% (Fig. 5b). The tropical  
407 Indian and Eastern Pacific Ocean are among the locations benefiting the most from the largest performance improvement,  
408 which highlights the skill of pattern filtering to remove variability associated with large climate modes (e.g., ENSO has a  
409 large influence on sea level in the Eastern Pacific Ocean). Similar to previous findings when using averaging (Fig. 4c),  
410 pattern filtering offers a reduced improvement in areas where regression already performed relatively well or where the  
411 presence of meso-scale processes is significant. Regardless of improvement magnitude, pattern filtering provides an overall  
412 increase in regression performance that is observable in the entire ocean domain. While averaging also offers an  
413 enhancement of pattern scaling skill, filtered 2-member pairs produce a distribution of RMSE that is significantly superior  
414 (Fig. 5c).

415 We further investigate how pattern filtering enhances regression compared to averaging by increasing the number of  
416 members included in the analysis (Fig. 5d). Increasing the number of realizations grants ensemble averaging a considerable  
417 decrease in RSME. Yet, performance improvement asymptotically reaches a plateau around 20 members after which further  
418 reductions in RMSE are modest. Regression based on pattern-filtered DSL also shows an improvement as the number of  
419 realizations increases. Such improvement is very limited compared to the one undergone by averaging, although filtering  
420 always provides a superior performance regardless of the number of members incorporated in the analysis. Importantly, area-  
421 weighted RMSE values differ significantly between the considered approaches when only a small number of realizations are  
422 available and become more similar for a larger number. This highlights the role of pattern filtering techniques when only a  
423 few ensemble members are available. Based on the analysis performed on the DSL simulations from the MPI-GE, filtering  
424 two members provides a regression performance that would only be achieved by averaging at least 12 members.

425





426

427 **Figure 5.** Regional pattern scaling performance based on regression RMSE when two ensemble members are used to estimate  
428 the forced response via S/N M EOF pattern filtering (a). Panel (b) shows the difference in regression performance between the  
429 2-member average pattern scaling (Fig. 4b) and the S/N M EOF-filtered equivalent (a). Violin plots depicting RMSE  
430 distributions from the 1-member, 2-member average, and 2-member S/N M EOF-filtered approaches are shown in panel (c).  
431 The area weighted average RMSE obtained in the regression is shown in (d) as a function of the number ensemble members  
432 included when using an ensemble mean (yellow) and filtering (blue). The difference in performances in terms of percentage  
433 is shown in green. Realizations used here belong to the RCP 2.6 scenario (we observed no discernible differences between  
434 scenarios).

435

### 436 4.3 Improved Pattern Scaling Using Single Realizations

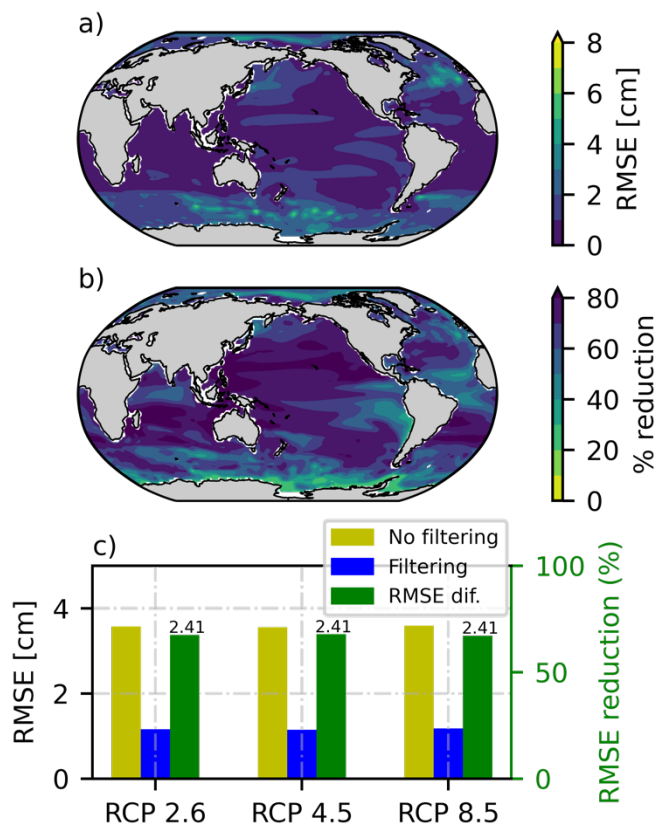
437 Most models in CMIP prior to CMIP6 provided only one realization of historical and scenario simulations. Therefore, we now  
438 test whether pattern filtering could improve regional emulation of single-realization models. To do so, we apply LFCA which  
439 uses a similar approach to S/N M EOF (as explained in Section 3.1.2). In this section, we first examine how LFCA improves  
440 the regression RMSE by truncating internal variability in a single simulation from the MPI-GE. We then apply LFCA to a



441 range of CMIP5 models that were used in previous patterns scaling analyses of DSL, focusing on the differences between  
442 models and RCP scenarios in longer simulations.

443 LFCA filtering uses the same linear algebra machinery as S/N M EOF, providing a similar regional improvement in pattern  
444 scaling (compare Fig. 5a and 6a). Slightly higher RMSE values are observed in LFCA-based regression, for instance, in the  
445 equatorial Pacific. This is expected because only one simulation is used, compared to two simulations in S/N M EOF filtering,  
446 which enables the latter to identify a larger proportion of internal variability. LFCA provides a substantial reduction in RMSE,  
447 as compared to using a single simulation in pattern scaling (Fig. 6b-c). Regionally, it shows a similar qualitative pattern of  
448 improvement as the other methods shown here (Fig. 6b vs 4c and 5b; averaging and S/N M EOF filtering, respectively).  
449 Quantitatively, however, LFCA provides a larger RMSE reduction on a single realization than S/N M EOF performed on two.  
450 LFCA provides a reduction of the area weighted average RMSE of 68% for all radiative forcing scenarios (Fig. 6c), while S/N  
451 M EOF yields 67% when using two realizations relative to unfiltered 1-member pattern scaling. While both estimates are quite  
452 similar, it is worth noting that S/N M EOF requires two ensemble members to provide such reduction, while LFCA leads to a  
453 similar performance just using one simulation. Similar to S/N M EOF pattern filtering, no substantial differences are found in  
454 pattern scaling RMSE between RCP scenarios up to 2100 (Fig., 6c). This implies that the relationship between DSL and  
455 GMTSLR is analogous between RCP scenarios, hence, a linear regression for projecting DSL leads to a similar performance  
456 for all RCPs both globally (Fig. 6c) and regionally (not shown).

457



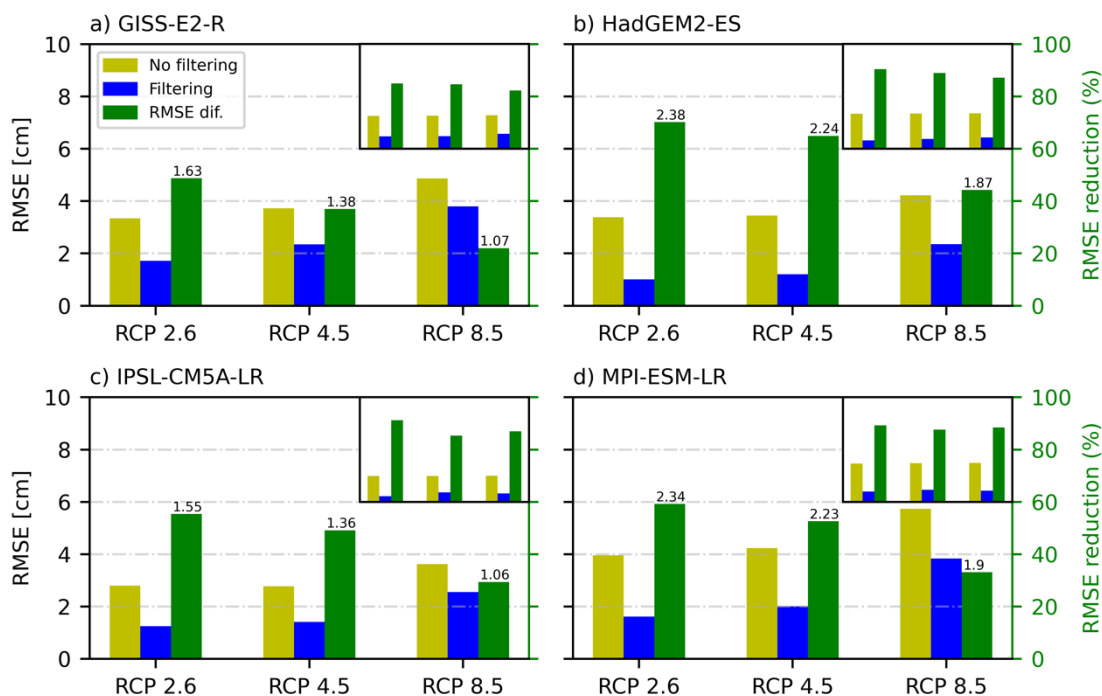
458

459 **Figure 6.** Regional pattern scaling performance based on regression RMSE when one (RCP 2.6) ensemble member is filtered  
 460 via LFCA (a). Filtering is performed individually for each ensemble member to compute 100 scaling patterns whose results  
 461 are averaged to diminish sampling issues. Differences in regression performance between Fig. 4a (unfiltered 1-member pattern  
 462 scaling) and (a) are shown in (b) in terms of percentage. The area-weighted average RMSE is shown in (c) for RCPs 2.6, 4.5,  
 463 and 8.5 and depending on whether the ensemble member is (blue) or not (yellow) filtered. Green indicates RMSE reduction  
 464 between approaches in terms of percentage, whereas values on top of the bars are the absolute differences in cm.

465 We further explore the performance of LFCA by comparing the pattern scaling results when isolating the forced response for  
 466 other GCMs. We identify the forced DSL in four CMIP5 models, being GISS-E2-R, HadGEM2-ES, IPSL-CM5A-LR, and  
 467 MPI-ESM-LR (Fig. 7a-d, respectively), which all provide scenario simulations up to 2300. To ease comparison with results  
 468 from the MPI-GE, however, we first examine results up to 2100 (Fig. 7a-d, small r.h.s. insets). RMSE from unfiltered  
 469 simulations up to 2100 vary between models, and so does RMSE reduction provided by LFCA. Nonetheless, error reduction  
 470 within a model and between scenarios is very similar, as previously observed for the MPI-GE. This implies that, for all models  
 471 considered here, there are no significant changing behaviours in the relationship between DSL and GMTLSR between RCP  
 472 scenarios up to 2100.



473 When considering results up to 2300, pattern scaling of unfiltered DSL against GMTSLR yields similar results as previous  
 474 studies (Bilbao et al., 2015), showing a global area-weighted mean RMSE between 2 and 4 cm. RMSE in both unfiltered and  
 475 filtered simulations of DSL increases with radiative forcing for all models considered. As simulations run up to 2300, a  
 476 decrease in pattern scaling performance for higher RCPs may indicate a more important role of the deeper ocean layer driving  
 477 non-linear processes (Bilbao et al., 2015; Yuan and Kopp, 2021). This tendency is also reflected in the error reduction after  
 478 filtering, which decreases as radiative forcing increases both over time and because of the higher emissions scenario, but the  
 479 latter is more apparent. Although LCFA filtering improves the performance of pattern scaling for all four CMIP5 models,  
 480 considerable differences in error reductions are observed. For instance, HadGEM2-ES benefits the most from pattern filtering  
 481 between all the models, with a ~70% decrease in error for RCP 2.6. Conversely, GISS-E2-R undergoes the lowest reduction  
 482 after pattern filtering, with about a 50% increase in performance for the same RCP scenario. Differences in model performance  
 483 pre- and post-filtering do not only highlight differences in how natural variability is represented in distinct models but may  
 484 also reflect model differences in terms of physics representation and modelled forced response.  
 485



486  
 487 **Figure 7.** Area-weighted average RMSE is shown for RCP 2.6, 4.5, and 8.5 and depending on whether the ensemble member  
 488 is (blue) or is not (yellow) filtered via LFCA. Green indicates RMSE reduction between approaches in terms of percentage,  
 489 whereas values on top of the bars are the absolute differences in cm. Different panels represent different CMIP5 models



490 considered here, as stated on top of each panel. The main panel includes simulation data up to 2300, whereas the small inset  
491 on the right-hand top corner shows RMSE results up to 2100.

## 492 **5 Conclusions**

493 Regional emulation tools for DSL change are complementary approaches to GCMs that allow for computationally cheap  
494 statistical projections. Most DSL regional emulators are based on pattern scaling, a statistical model usually based on a grid-  
495 point regression against a global variable representing change in the climate system driven by external forcing. While choosing  
496 suitable global predictors is essential for appropriate tuning of the statistical model, random errors can remain leading to high  
497 uncertainties in statistically based projections. A portion of these random errors are driven by internal variability in DSL and  
498 can be characterised using macro-initialized initial condition large ensembles (SMILES), which are designed to facilitate a  
499 separation between internal variability and external forcings within a model. Here, we applied pattern recognition techniques  
500 to a SMILE with the aim to efficiently truncate internal variability and demonstrate how these approaches could significantly  
501 reduce random errors in regional emulators of DSL.

502 Although internal variability can be also reduced by using more conventional methods, such as computing an ensemble mean  
503 or linear trends, this requires a relatively large number of realizations to do it effectively. This is a significant constraint  
504 particularly for modelling experiments featuring a limited number of realizations. A more efficient alternative consists of  
505 employing methods that exploit spatial covariance information, such as S/N M EOF pattern filtering. We have demonstrated  
506 that S/N M EOF applied to two realizations attains the same level of error reduction as averaging 12 realizations. The largest  
507 improvement relative to unfiltered simulations was observed when only a few simulations were available, whereas both S/N-  
508 filtered and ensemble average model performance tended to converge for a large number of ensemble members. By identifying  
509 spatiotemporal coherent structures, the S/N M EOF filtering was particularly skilful at removing internal variability due to  
510 large modes of climate variability, such as the ENSO influence on sea level in the Eastern Pacific.

511 S/N M EOF pattern filtering can identify the common response within at least two realizations. This motivated us to also test  
512 LFCA, which can remove variability in single realization modelling experiments by applying a lowpass filter. Apart from  
513 being computationally more efficient, LFCA outperforms S/N M EOF in improving the performance of DSL pattern scaling  
514 when using one or two realizations. However, previous studies have emphasized that S/N M EOF pattern filtering provides a  
515 range of benefits compared to LFCA, including: 1) a better isolation of the forced response when the number of ensemble  
516 members is large, and 2) the detection of relatively less important forced patterns, such as those driven by volcanism.

517 We have also investigated LFCA by applying it to longer (up to 2300) CMIP5 simulations. We found that pattern scaling  
518 performance is independent of the GHG emission scenario up to 2100 and decreases with radiative forcing beyond 2100. Since  
519 we used a linear model, this implies that non-linear processes have different effects on DSL depending on the GHG scenario  
520 and this is reflected in a decrease in model performance depending on the emissions. We also found substantial differences  
521 between CMIP5 models, due to variability being represented differently as well as distinct model physics. Nonetheless, the



522 performance improvement of pattern scaling when applying LFCA filtering is considerable for all models and scenarios,  
523 ranging from 20% to more than 70% reduction relative to the unfiltered results.  
524 Here, we have demonstrated that reducing internal variability increases the capabilities of statistical approaches to project  
525 DSL. Pattern recognition techniques are especially advantageous for such a task, as they do not require numerous realizations  
526 to significantly reduce uncertainties in statistical projections and no data is lost (as in 30-year means) when reducing internal  
527 variability. Previous studies have not considered removing internal variability prior to searching for suitable global predictors,  
528 which could significantly reduce uncertainties in statistically projected DSL. Hence, for future emulation studies of DSL, we  
529 recommend pattern filtering as a pre-processing step before selecting suitable predictors.

### 530 **Code availability**

531 The methods used to perform this study are an adaptation from the ones used by Wills et al. (2020). The code is available at  
532 <https://github.com/rcjwills/forced-patterns> and <https://github.com/rcjwills/lfca>.

### 533 **Data availability**

534 Simulations from the MPI-GE can be obtained at <https://esgf-data.dkrz.de/projects/mip-ge/>, whereas CMIP5 data can be found  
535 at <https://esgf-node.llnl.gov/search/cmip5/>.

### 536 **Author contribution**

537 VMS devised, designed, and performed the analysis, and wrote the manuscript. ABAS supervised the study and contributed  
538 to writing. THJH contributed to data pre-processing and manuscript writing. SD and MM provided valuable feedback on  
539 methods and contributed to writing. NM provided useful information on the use of the MPI-GE.

### 540 **Competing interests**

541 The authors declare that they have no conflict of interest.

### 542 **Acknowledgements**

543 VMS, ABAS, THJH were supported by PROTECT. This project has received funding from the European Union's Horizon  
544 2020 research and innovation programme under grant agreement No 869304. SD acknowledges David and Jane Flowerree for  
545 their support. We acknowledge the World Climate Research Programme's Working Group on Coupled Modelling, which is  
546 responsible for CMIP, and we thank the climate modelling groups for producing and making available their model output. For



547 CMIP the U.S. Department of Energy’s Program for Climate Model Diagnosis and Intercomparison provides coordinating  
548 support and led development of software infrastructure in partnership with the Global Organization for Earth System Science  
549 Portals.

## 550 **References**

551 Becker, M., Karpytchev, M., and Lennartz-Sassinek, S.: Long-term sea level trends: Natural or anthropogenic?, *Geophysical*  
552 *Research Letters*, 41, 5571–5580, <https://doi.org/10.1002/2014GL061027>, 2014.

553 Bilbao, R. A. F., Gregory, J. M., and Bouttes, N.: Analysis of the regional pattern of sea level change due to ocean dynamics  
554 and density change for 1993–2099 in observations and CMIP5 AOGCMs, *Clim Dyn*, 45, 2647–2666,  
555 <https://doi.org/10.1007/s00382-015-2499-z>, 2015.

556 Bouttes, N., Gregory, J. M., Kuhlbrodt, T., and Smith, R. S.: The drivers of projected North Atlantic sea level change, *Clim*  
557 *Dyn*, 43, 1531–1544, <https://doi.org/10.1007/s00382-013-1973-8>, 2014.

558 Church, J. A., Clark, P. U., Cazenave, A., Gregory, J. M., Jevrejeva, S., Levermann, A., Merrifield, M. A., Milne, G. A.,  
559 Nerem, R. S., and Nunn, P. D.: *Sea level change*, PM Cambridge University Press, 2013.

560 Collins, M., Knutti, R., Arblaster, J., Dufresne, J.-L., Fichet, T., Friedlingstein, P., Gao, X., Gutowski, W. J., Johns, T.,  
561 Krinner, G., Shongwe, M., Tebaldi, C., Weaver, A. J., Wehner, M. F., Allen, M. R., Andrews, T., Beyerle, U., Bitz, C. M.,  
562 Bony, S., and Booth, B. B. B.: Long-term Climate Change: Projections, Commitments and Irreversibility, *Climate Change*  
563 *2013 - The Physical Science Basis: Contribution of Working Group I to the Fifth Assessment Report of the Intergovernmental*  
564 *Panel on Climate Change*, 1029–1136, 2013.

565 Cooley, S., D. Schoeman, L. Bopp, P. Boyd, S. Donner, D.Y. Ghebrehiwet, S.-I. Ito, W. Kiessling, P. Martinetto, E. Ojea, M.-  
566 F. Racault, B. Rost, and M. Skern-Mauritzen: Ocean and Coastal Ecosystems and their Services. In: *Climate Change 2022:*  
567 *Impacts, Adaptation, and Vulnerability. Contribution of Working Group II to the Sixth Assessment Report of the*  
568 *Intergovernmental Panel on Climate Change* [H.-O. Pörtner, D.C. Roberts, M. Tignor, E.S. Poloczanska, K. Mintenbeck, A.  
569 Alegria, M. Craig, S. Langsdorf, S. Löschke, V. Möller, A. Okem, B. Rama (eds.)]. Cambridge University Press, Cambridge,  
570 UK and New York, NY, USA, pp. 379-550, doi:10.1017/9781009325844.005, 2022.

571 Couldrey, M. P., Gregory, J. M., Boeira Dias, F., Dobrohotoff, P., Domingues, C. M., Garuba, O., Griffies, S. M., Haak, H.,  
572 Hu, A., Ishii, M., Jungclaus, J., Köhl, A., Marsland, S. J., Ojha, S., Saenko, O. A., Savita, A., Shao, A., Stammer, D., Suzuki,



- 573 T., Todd, A., and Zanna, L.: What causes the spread of model projections of ocean dynamic sea-level change in response to  
574 greenhouse gas forcing?, *Clim Dyn*, 56, 155–187, <https://doi.org/10.1007/s00382-020-05471-4>, 2021.
- 575 Danabasoglu, G., Lamarque, J.-F., Bacmeister, J., Bailey, D. A., DuVivier, A. K., Edwards, J., Emmons, L. K., Fasullo, J.,  
576 Garcia, R., and Gettelman, A.: The community earth system model version 2 (CESM2), *Journal of Advances in Modeling  
577 Earth Systems*, 12, e2019MS001916, 2020.
- 578 Dangendorf, S., Rybski, D., Mudersbach, C., Müller, A., Kaufmann, E., Zorita, E., and Jensen, J.: Evidence for long-term  
579 memory in sea level, *Geophysical Research Letters*, 41, 5530–5537, <https://doi.org/10.1002/2014GL060538>, 2014.
- 580 Dangendorf, S., Hay, C., Calafat, F. M., Marcos, M., Piecuch, C. G., Berk, K., and Jensen, J.: Persistent acceleration in global  
581 sea-level rise since the 1960s, *Nat. Clim. Chang.*, 9, 705–710, <https://doi.org/10.1038/s41558-019-0531-8>, 2019.
- 582 DelSole, T., Tippett, M. K., and Shukla, J.: A significant component of unforced multidecadal variability in the recent  
583 acceleration of global warming, *Journal of Climate*, 24, 909–926, 2011.
- 584 Deser, C., Lehner, F., Rodgers, K. B., Ault, T., Delworth, T. L., DiNezio, P. N., Fiore, A., Frankignoul, C., Fyfe, J. C., Horton,  
585 D. E., Kay, J. E., Knutti, R., Lovenduski, N. S., Marotzke, J., McKinnon, K. A., Minobe, S., Randerson, J., Screen, J. A.,  
586 Simpson, I. R., and Ting, M.: Insights from Earth system model initial-condition large ensembles and future prospects, *Nat.  
587 Clim. Chang.*, 10, 277–286, <https://doi.org/10.1038/s41558-020-0731-2>, 2020.
- 588 Duchon, C. E.: Lanczos Filtering in One and Two Dimensions, *Journal of Applied Meteorology and Climatology*, 18, 1016–  
589 1022, [https://doi.org/10.1175/1520-0450\(1979\)018<1016:LFIOAT>2.0.CO;2](https://doi.org/10.1175/1520-0450(1979)018<1016:LFIOAT>2.0.CO;2), 1979.
- 590 Eyring, V., Bony, S., Meehl, G. A., Senior, C. A., Stevens, B., Stouffer, R. J., and Taylor, K. E.: Overview of the Coupled  
591 Model Intercomparison Project Phase 6 (CMIP6) experimental design and organization, *Geoscientific Model Development*,  
592 9, 1937–1958, <https://doi.org/10.5194/gmd-9-1937-2016>, 2016.
- 593 Farrell, W. E. and Clark, J. A.: On postglacial sea level, *Geophysical Journal International*, 46, 647–667, 1976.
- 594 Fasullo, J. T., Gent, P. R., and Nerem, R. S.: Forced Patterns of Sea Level Rise in the Community Earth System Model Large  
595 Ensemble From 1920 to 2100, *Journal of Geophysical Research: Oceans*, 125, e2019JC016030,  
596 <https://doi.org/10.1029/2019JC016030>, 2020.
- 597 Ferrero, B., Tonelli, M., Marcello, F., and Wainer, I.: Long-term Regional Dynamic Sea Level Changes from CMIP6  
598 Projections, *Adv. Atmos. Sci.*, 38, 157–167, <https://doi.org/10.1007/s00376-020-0178-4>, 2021.





- 599 Fox-Kemper, B., H.T. Hewitt, C. Xiao, G. Aðalgeirsdóttir, S.S. Drijfhout, T.L. Edwards, N.R. Golledge, M. Hemer, R.E.  
600 Kopp, G. Krinner, A. Mix, D. Notz, S. Nowicki, I.S. Nurhati, L. Ruiz, J.-B. Sallée, A.B.A. Slangen, and Y. Yu: Ocean,  
601 Cryosphere and Sea Level Change. In *Climate Change 2021: The Physical Science Basis. Contribution of Working Group I  
602 to the Sixth Assessment Report of the Intergovernmental Panel on Climate Change* [Masson-Delmotte, V., P. Zhai, A. Pirani,  
603 S.L. Connors, C. Péan, S. Berger, N. Caud, Y. Chen, L. Goldfarb, M.I. Gomis, M. Huang, K. Leitzell, E. Lonnoy, J.B.R.  
604 Matthews, T.K. Maycock, T. Waterfield, O. Yelekçi, R. Yu, and B. Zhou (eds.)]. Cambridge University Press, Cambridge,  
605 United Kingdom and New York, NY, USA, pp. 1211–1362, doi:10.1017/9781009157896.011, 2021.
- 606 Frankcombe, L. M., Spence, P., Hogg, A. M., England, M. H., and Griffies, S. M.: Sea level changes forced by Southern Ocean  
607 winds, *Geophysical Research Letters*, 40, 5710–5715, 2013.
- 608 Frankcombe, L. M., England, M. H., Mann, M. E., and Steinman, B. A.: Separating Internal Variability from the Externally  
609 Forced Climate Response, *Journal of Climate*, 28, 8184–8202, <https://doi.org/10.1175/JCLI-D-15-0069.1>, 2015.
- 610 Frederikse, T., Landerer, F., Caron, L., Adhikari, S., Parkes, D., Humphrey, V. W., Dangendorf, S., Hogarth, P., Zanna, L.,  
611 and Cheng, L.: The causes of sea-level rise since 1900, *Nature*, 584, 393–397, 2020.
- 612 Geoffroy, O., Saint-Martin, D., Olivié, D. J., Voldoire, A., Bellon, G., and Tytéca, S.: Transient climate response in a two-  
613 layer energy-balance model. Part I: Analytical solution and parameter calibration using CMIP5 AOGCM experiments, *Journal  
614 of Climate*, 26, 1841–1857, 2013a.
- 615 Geoffroy, O., Saint-Martin, D., Bellon, G., Voldoire, A., Olivié, D. J. L., and Tytéca, S.: Transient climate response in a two-  
616 layer energy-balance model. Part II: Representation of the efficacy of deep-ocean heat uptake and validation for CMIP5  
617 AOGCMs, *Journal of Climate*, 26, 1859–1876, 2013b.
- 618 Goodwin, P., Katavouta, A., Roussenov, V. M., Foster, G. L., Rohling, E. J., and Williams, R. G.: Pathways to 1.5 C and 2 C  
619 warming based on observational and geological constraints, *Nature Geoscience*, 11, 102–107, 2018.
- 620 Gregory, J. M., Griffies, S. M., Hughes, C. W., Lowe, J. A., Church, J. A., Fukimori, I., Gomez, N., Kopp, R. E., Landerer, F.,  
621 Cozannet, G. L., Ponte, R. M., Stammer, D., Tamisiea, M. E., and van de Wal, R. S. W.: Concepts and Terminology for Sea  
622 Level: Mean, Variability and Change, Both Local and Global, *Surv Geophys*, 40, 1251–1289, [https://doi.org/10.1007/s10712-  
623 019-09525-z](https://doi.org/10.1007/s10712-019-09525-z), 2019.
- 624 Griffies, S. M., Danabasoglu, G., Durack, P. J., Adcroft, A. J., Balaji, V., Böning, C. W., Chassignet, E. P., Curchitser, E.,  
625 Deshayes, J., Drange, H., Fox-Kemper, B., Gleckler, P. J., Gregory, J. M., Haak, H., Hallberg, R. W., Heimbach, P., Hewitt,  
626 H. T., Holland, D. M., Ilyina, T., Jungclaus, J. H., Komuro, Y., Krasting, J. P., Large, W. G., Marsland, S. J., Masina, S.,



- 627 McDougall, T. J., Nurser, A. J. G., Orr, J. C., Pirani, A., Qiao, F., Stouffer, R. J., Taylor, K. E., Treguier, A. M., Tsujino, H.,  
628 Uotila, P., Valdivieso, M., Wang, Q., Winton, M., and Yeager, S. G.: OMIP contribution to CMIP6: experimental and  
629 diagnostic protocol for the physical component of the Ocean Model Intercomparison Project, *Geoscientific Model*  
630 *Development*, 9, 3231–3296, <https://doi.org/10.5194/gmd-9-3231-2016>, 2016.
- 631 Haasnoot, M., Brown, S., Scussolini, P., Jimenez, J. A., Vafeidis, A. T., and Nicholls, R. J.: Generic adaptation pathways for  
632 coastal archetypes under uncertain sea-level rise, *Environmental Research Communications*, 1, 071006, 2019.
- 633 Haasnoot, M., Winter, G., Brown, S., Dawson, R. J., Ward, P. J., and Eilander, D.: Long-term sea-level rise necessitates a  
634 commitment to adaptation: A first order assessment, *Climate Risk Management*, 34, 100355,  
635 <https://doi.org/10.1016/j.crm.2021.100355>, 2021.
- 636 Haigh, I. D., Pickering, M. D., Green, J. A. M., Arbic, B. K., Arns, A., Dangendorf, S., Hill, D. F., Horsburgh, K., Howard,  
637 T., Idier, D., Jay, D. A., Jänicke, L., Lee, S. B., Müller, M., Schindelegger, M., Talke, S. A., Wilmes, S.-B., and Woodworth,  
638 P. L.: The Tides They Are A-Changin’: A Comprehensive Review of Past and Future Nonastronomical Changes in Tides,  
639 Their Driving Mechanisms, and Future Implications, *Reviews of Geophysics*, 58, e2018RG000636,  
640 <https://doi.org/10.1029/2018RG000636>, 2020.
- 641 Hawkins, E. and Sutton, R.: Time of emergence of climate signals, *Geophysical Research Letters*, 39,  
642 <https://doi.org/10.1029/2011GL050087>, 2012.
- 643 Hawkins, E., Smith, R. S., Gregory, J. M., and Stainforth, D. A.: Irreducible uncertainty in near-term climate projections, *Clim*  
644 *Dyn*, 46, 3807–3819, <https://doi.org/10.1007/s00382-015-2806-8>, 2016.
- 645 Herger, N., Sanderson, B. M., and Knutti, R.: Improved pattern scaling approaches for the use in climate impact studies,  
646 *Geophysical Research Letters*, 42, 3486–3494, <https://doi.org/10.1002/2015GL063569>, 2015.
- 647 Hermans, T. H. J., Tinker, J., Palmer, M. D., Katsman, C. A., Vermeersen, B. L. A., and Slangen, A. B. A.: Improving sea-  
648 level projections on the Northwestern European shelf using dynamical downscaling, *Clim Dyn*, 54, 1987–2011,  
649 <https://doi.org/10.1007/s00382-019-05104-5>, 2020.
- 650 Hinkel, J., Lincke, D., Vafeidis, A. T., Perrette, M., Nicholls, R. J., Tol, R. S., Marzeion, B., Fettweis, X., Ionescu, C., and  
651 Levermann, A.: Coastal flood damage and adaptation costs under 21st century sea-level rise, *Proceedings of the National*  
652 *Academy of Sciences*, 111, 3292–3297, 2014.



- 653 Hobbs, W., Palmer, M. D., and Monselesan, D.: An energy conservation analysis of ocean drift in the CMIP5 global coupled  
654 models, *Journal of Climate*, 29, 1639–1653, 2016.
- 655 Imawaki, S., Bower, A. S., Beal, L., and Qiu, B.: Chapter 13 - Western Boundary Currents, in: *International Geophysics*, vol.  
656 103, edited by: Siedler, G., Griffies, S. M., Gould, J., and Church, J. A., Academic Press, 305–338,  
657 <https://doi.org/10.1016/B978-0-12-391851-2.00013-1>, 2013.
- 658 Kay, J. E., Deser, C., Phillips, A., Mai, A., Hannay, C., Strand, G., Arblaster, J. M., Bates, S. C., Danabasoglu, G., and Edwards,  
659 J.: The Community Earth System Model (CESM) large ensemble project: A community resource for studying climate change  
660 in the presence of internal climate variability, *Bulletin of the American Meteorological Society*, 96, 1333–1349, 2015.
- 661 Labe, Z. M. and Barnes, E. A.: Detecting Climate Signals Using Explainable AI With Single-Forcing Large Ensembles, *Journal*  
662 *of Advances in Modeling Earth Systems*, 13, e2021MS002464, <https://doi.org/10.1029/2021MS002464>, 2021.
- 663 Landerer, F. W., Jungclauss, J. H., and Marotzke, J.: Regional dynamic and steric sea level change in response to the IPCC-  
664 A1B scenario, *Journal of Physical Oceanography*, 37, 296–312, 2007.
- 665 Lowe, J. A. and Gregory, J. M.: Understanding projections of sea level rise in a Hadley Centre coupled climate model, *Journal*  
666 *of Geophysical Research: Oceans*, 111, 2006.
- 667 Lyu, K., Zhang, X., and Church, J. A.: Regional Dynamic Sea Level Simulated in the CMIP5 and CMIP6 Models: Mean  
668 Biases, Future Projections, and Their Linkages, *Journal of Climate*, 33, 6377–6398, <https://doi.org/10.1175/JCLI-D-19-1029.1>,  
669 2020.
- 670 Maher, N., Milinski, S., Suarez-Gutierrez, L., Botzet, M., Dobrynin, M., Kornbluh, L., Kröger, J., Takano, Y., Ghosh, R.,  
671 Hedemann, C., Li, C., Li, H., Manzini, E., Notz, D., Putrasahan, D., Boysen, L., Claussen, M., Ilyina, T., Olonscheck, D.,  
672 Raddatz, T., Stevens, B., and Marotzke, J.: The Max Planck Institute Grand Ensemble: Enabling the Exploration of Climate  
673 System Variability, *Journal of Advances in Modeling Earth Systems*, 11, 2050–2069, <https://doi.org/10.1029/2019MS001639>,  
674 2019.
- 675 Maher, N., Milinski, S., and Ludwig, R.: Large ensemble climate model simulations: introduction, overview, and future  
676 prospects for utilising multiple types of large ensemble, *Earth System Dynamics*, 12, 401–418, <https://doi.org/10.5194/esd-12-401-2021>, 2021a.  
677



- 678 Maher, N., Power, S., and Marotzke, J.: More accurate quantification of model-to-model agreement in externally forced  
679 climatic responses over the coming century, *Nature Communications*, 12, 788, <https://doi.org/10.1038/s41467-020-20635-w>,  
680 2021b.
- 681 Mankin, J. S., Lehner, F., Coats, S., and McKinnon, K. A.: The Value of Initial Condition Large Ensembles to Robust  
682 Adaptation Decision-Making, *Earth's Future*, 8, e2012EF001610, <https://doi.org/10.1029/2020EF001610>, 2020.
- 683 Marcos, M. and Amores, A.: Quantifying anthropogenic and natural contributions to thermosteric sea level rise, *Geophysical*  
684 *Research Letters*, 41, 2502–2507, <https://doi.org/10.1002/2014GL059766>, 2014.
- 685 Meinshausen, M., Raper, S. C. B., and Wigley, T. M. L.: Emulating coupled atmosphere-ocean and carbon cycle models with  
686 a simpler model, *MAGICC6 – Part 1: Model description and calibration*, *Atmospheric Chemistry and Physics*, 11, 1417–1456,  
687 <https://doi.org/10.5194/acp-11-1417-2011>, 2011.
- 688 Millar, R. J., Nicholls, Z. R., Friedlingstein, P., and Allen, M. R.: A modified impulse-response representation of the global  
689 near-surface air temperature and atmospheric concentration response to carbon dioxide emissions, *Atmospheric Chemistry and*  
690 *Physics*, 17, 7213–7228, 2017.
- 691 Mitchell, T. D.: Pattern Scaling: An Examination of the Accuracy of the Technique for Describing Future Climates, *Climatic*  
692 *Change*, 60, 217–242, <https://doi.org/10.1023/A:1026035305597>, 2003.
- 693 Mitrovica, J. X., Tamisiea, M. E., Davis, J. L., and Milne, G. A.: Recent mass balance of polar ice sheets inferred from patterns  
694 of global sea-level change, *Nature*, 409, 1026–1029, 2001.
- 695 Moftakhari, H. R., AghaKouchak, A., Sanders, B. F., Feldman, D. L., Sweet, W., Matthew, R. A., and Luke, A.: Increased  
696 nuisance flooding along the coasts of the United States due to sea level rise: Past and future, *Geophysical Research Letters*,  
697 42, 9846–9852, 2015.
- 698 Nerem, R. S., Leuliette, É., and Cazenave, A.: Present-day sea-level change: A review, *Comptes Rendus Geoscience*, 338,  
699 1077–1083, <https://doi.org/10.1016/j.crte.2006.09.001>, 2006.
- 700 Nicholls, R. J., Lincke, D., Hinkel, J., Brown, S., Vafeidis, A. T., Meyssignac, B., Hanson, S. E., Merkens, J.-L., and Fang, J.:  
701 A global analysis of subsidence, relative sea-level change and coastal flood exposure, *Nature Climate Change*, 11, 338–342,  
702 <https://doi.org/10.1038/s41558-021-00993-z>, 2021.
- 703 O'Neill, B. C., Kriegler, E., Ebi, K. L., Kemp-Benedict, E., Riahi, K., Rothman, D. S., van Ruijven, B. J., van Vuuren, D. P.,  
704 Birkmann, J., Kok, K., Levy, M., and Solecki, W.: The roads ahead: Narratives for shared socioeconomic pathways describing



- 705 world futures in the 21st century, *Global Environmental Change*, 42, 169–180,  
706 <https://doi.org/10.1016/j.gloenvcha.2015.01.004>, 2017.
- 707 Osborn, T. J., Wallace, C. J., Harris, I. C., and Melvin, T. M.: Pattern scaling using ClimGen: monthly-resolution future climate  
708 scenarios including changes in the variability of precipitation, *Climatic Change*, 134, 353–369, [https://doi.org/10.1007/s10584-](https://doi.org/10.1007/s10584-015-1509-9)  
709 015-1509-9, 2016.
- 710 Peltier, W. R.: Global sea level rise and glacial isostatic adjustment, *Global and Planetary Change*, 20, 93–123, 1999.
- 711 Peltier, W. R.: Global glacial isostatic adjustment and modern instrumental records of relative sea level history, in: *International*  
712 *geophysics*, vol. 75, Elsevier, 65–95, 2001.
- 713 Perrette, M., Landerer, F., Riva, R., Frieler, K., and Meinshausen, M.: A scaling approach to project regional sea level rise and  
714 its uncertainties, *Earth System Dynamics*, 4, 11–29, 2013.
- 715 Riahi, K., van Vuuren, D. P., Kriegler, E., Edmonds, J., O’Neill, B. C., Fujimori, S., Bauer, N., Calvin, K., Dellink, R., Fricko,  
716 O., Lutz, W., Popp, A., Cuaresma, J. C., Kc, S., Leimbach, M., Jiang, L., Kram, T., Rao, S., Emmerling, J., Ebi, K., Hasegawa,  
717 T., Havlik, P., Humpenöder, F., Da Silva, L. A., Smith, S., Stehfest, E., Bosetti, V., Eom, J., Gernaat, D., Masui, T., Rogelj,  
718 J., Strefler, J., Drouet, L., Krey, V., Luderer, G., Harmsen, M., Takahashi, K., Baumstark, L., Doelman, J. C., Kainuma, M.,  
719 Klimont, Z., Marangoni, G., Lotze-Campen, H., Obersteiner, M., Tabeau, A., and Tavoni, M.: The Shared Socioeconomic  
720 Pathways and their energy, land use, and greenhouse gas emissions implications: An overview, *Global Environmental Change*,  
721 42, 153–168, <https://doi.org/10.1016/j.gloenvcha.2016.05.009>, 2017.
- 722 Rintoul, S., Hughes, C., and Olbers, D.: Chapter 4.6 The antarctic circumpolar current system, in: *International Geophysics*,  
723 vol. 77, edited by: Siedler, G., Church, J., and Gould, J., Academic Press, 271–XXXVI, [https://doi.org/10.1016/S0074-](https://doi.org/10.1016/S0074-6142(01)80124-8)  
724 6142(01)80124-8, 2001.
- 725 Santer, B. D., Wigley, T. M., Schlesinger, M. E., and Mitchell, J. F.: Developing climate scenarios from equilibrium GCM  
726 results, 1990.
- 727 Schneider, T. and Griffies, S. M.: A conceptual framework for predictability studies, *Journal of climate*, 12, 3133–3155, 1999.
- 728 Schneider, T. and Held, I. M.: Discriminants of twentieth-century changes in Earth surface temperatures, *Journal of Climate*,  
729 14, 249–254, 2001.
- 730 Sen Gupta, A. S., Jourdain, N. C., Brown, J. N., and Monselesan, D.: Climate drift in the CMIP5 models, *Journal of Climate*,  
731 26, 8597–8615, 2013.



- 732 Slangen, A. B. A., Carson, M., Katsman, C. A., Van de Wal, R. S. W., Köhl, A., Vermeersen, L. L. A., and Stammer, D.:  
733 Projecting twenty-first century regional sea-level changes, *Climatic Change*, 124, 317–332, 2014.
- 734 Slangen, A. B. A., Adloff, F., Jevrejeva, S., Leclercq, P. W., Marzeion, B., Wada, Y., and Winkelmann, R.: A Review of  
735 Recent Updates of Sea-Level Projections at Global and Regional Scales, *Surv Geophys*, 38, 385–406,  
736 <https://doi.org/10.1007/s10712-016-9374-2>, 2017.
- 737 Smith, C. J., Forster, P. M., Allen, M., Leach, N., Millar, R. J., Passerello, G. A., and Regayre, L. A.: FAIR v1. 3: a simple  
738 emissions-based impulse response and carbon cycle model, *Geoscientific Model Development*, 11, 2273–2297, 2018.
- 739 Stainforth, D. a, Allen, M. r, Tredger, E. r, and Smith, L. a: Confidence, uncertainty and decision-support relevance in climate  
740 predictions, *Philosophical Transactions of the Royal Society A: Mathematical, Physical and Engineering Sciences*, 365, 2145–  
741 2161, <https://doi.org/10.1098/rsta.2007.2074>, 2007.
- 742 Stammer, D. and Hüttemann, S.: Response of regional sea level to atmospheric pressure loading in a climate change scenario,  
743 *Journal of Climate*, 21, 2093–2101, 2008.
- 744 Steffebauer, D. B., Riva, R. E. M., Timmermans, J. S., Kwakkel, J. H., and Bakker, M.: Evidence of regional sea-level rise  
745 acceleration for the North Sea, *Environ. Res. Lett.*, 17, 074002, <https://doi.org/10.1088/1748-9326/ac753a>, 2022.
- 746 Tebaldi, C. and Arblaster, J. M.: Pattern scaling: Its strengths and limitations, and an update on the latest model simulations,  
747 *Climatic Change*, 122, 459–471, <https://doi.org/10.1007/s10584-013-1032-9>, 2014.
- 748 Thomas, M. A. and Lin, T.: A dual model for emulation of thermosteric and dynamic sea-level change, *Climatic Change*, 148,  
749 311–324, 2018.
- 750 Ting, M., Kushnir, Y., Seager, R., and Li, C.: Forced and Internal Twentieth-Century SST Trends in the North Atlantic, *Journal*  
751 *of Climate*, 22, 1469–1481, <https://doi.org/10.1175/2008JCLI2561.1>, 2009.
- 752 Venzke, S., Allen, M. R., Sutton, R. T., and Rowell, D. P.: The atmospheric response over the North Atlantic to decadal  
753 changes in sea surface temperature, *Journal of Climate*, 12, 2562–2584, 1999.
- 754 Vitousek, S., Barnard, P. L., Fletcher, C. H., Frazer, N., Erikson, L., and Storlazzi, C. D.: Doubling of coastal flooding  
755 frequency within decades due to sea-level rise, *Scientific reports*, 7, 1–9, 2017.



- 756 van Vuuren, D. P., Edmonds, J., Kainuma, M., Riahi, K., Thomson, A., Hibbard, K., Hurtt, G. C., Kram, T., Krey, V.,  
757 Lamarque, J.-F., Masui, T., Meinshausen, M., Nakicenovic, N., Smith, S. J., and Rose, S. K.: The representative concentration  
758 pathways: an overview, *Climatic Change*, 109, 5, <https://doi.org/10.1007/s10584-011-0148-z>, 2011.
- 759 Wahl, T., Haigh, I. D., Nicholls, R. J., Arns, A., Dangendorf, S., Hinkel, J., and Slangen, A. B. A.: Understanding extreme sea  
760 levels for broad-scale coastal impact and adaptation analysis, *Nat Commun*, 8, 16075, <https://doi.org/10.1038/ncomms16075>,  
761 2017.
- 762 Wells, C. D., Jackson, L. S., Maycock, A. C., and Forster, P. M.: Understanding pattern scaling errors across a range of  
763 emissions pathways, 30, 2022.
- 764 Wills, R. C., Schneider, T., Wallace, J. M., Battisti, D. S., and Hartmann, D. L.: Disentangling Global Warming, Multidecadal  
765 Variability, and El Niño in Pacific Temperatures, *Geophysical Research Letters*, 45, 2487–2496,  
766 <https://doi.org/10.1002/2017GL076327>, 2018.
- 767 Wills, R. C. J., Battisti, D. S., Armour, K. C., Schneider, T., and Deser, C.: Pattern Recognition Methods to Separate Forced  
768 Responses from Internal Variability in Climate Model Ensembles and Observations, *Journal of Climate*, 33, 8693–8719,  
769 <https://doi.org/10.1175/JCLI-D-19-0855.1>, 2020.
- 770 Wu, Q., Zhang, X., Church, J. A., Hu, J., and Gregory, J. M.: Evolving patterns of steredynamic sea-level rise under mitigation  
771 scenarios and insights from linear system theory, *Clim Dyn*, 57, 635–656, <https://doi.org/10.1007/s00382-021-05727-7>, 2021.
- 772 Yuan, J. and Kopp, R. E.: Emulating Ocean Dynamic Sea Level by Two-Layer Pattern Scaling, *Journal of Advances in*  
773 *Modeling Earth Systems*, 13, e2020MS002323, <https://doi.org/10.1029/2020MS002323>, 2021.

774